Nucleic Acids Research, 2025, **53**, gkaf065
https://doi.org/10.1093/nar/gkaf065
Advance access publication date: 11 February 2025
Structural Biology

Allovalent scavenging of activation domains in the transcription factor ANAC013 gears transcriptional regulation

Elise Delaforge [1,2,3], Amanda D. Due [1,2,3], Frederik Friis Theisen [1,2,3], Nicolas Morffy[4], Charlotte O'Shea[2], Martin Blackledge[5], Lucia C. Strader[4], Karen Skriver [1,2,*], Birthe B. Kragelund [1,2,3,*]

[1]REPIN, Department of Biology, University of Copenhagen, Ole Maaløes vej 5, DK-2200 Copenhagen N, Denmark
[2]Linderstrøm-Lang Centre for Protein Science and Department of Biology, University of Copenhagen, Ole Maaløes vej 5, DK-2200 Copenhagen N, Denmark
[3]Structural Biology and NMR Laboratory, Department of Biology, University of Copenhagen, Ole Maaløes vej 5, DK-2200 Copenhagen N, Denmark
[4]Department of Biology, Duke University, 27708 Durham, NC, United States
[5]Université Grenoble Alpes, Le Centre National de la Recherche Scientifique, Commissariat à l'Energie Atomique et aux Energies Alternatives, Institut de Biologie Structurale, 38000 Grenoble, France

[*]To whom correspondence should be addressed. Email: bbk@bio.ku.dk
Correspondence may also be addressed to Karen Skriver. Email: kskriver@bio.ku.dk

Abstract

Transcriptional regulation involves interactions between transcription factors, coregulators, and DNA. Intrinsic disorder is a major player in this regulation, but mechanisms driven by disorder remain elusive. Here, we address molecular communication within the stress-regulating *Arabidopsis thaliana* transcription factor ANAC013. Through high-throughput screening of ANAC013 for transcriptional activation activity, we identify three activation domains within its C-terminal intrinsically disordered region. Two of these overlap with acidic islands and form dynamic interactions with the DNA-binding domain and are released, not only upon binding of target promoter DNA, but also by nonspecific DNA. We show that independently of DNA binding, the RST (RCD–SRO–TAF4) domain of the negative regulator RCD1 (Radical-induced Cell Death1) scavenges the two acidic activation domains positioned vis-à-vis through allovalent binding, leading to dynamic occupation at enhanced affinity. We propose an allovalency model for transcriptional regulation, where sequentially close activation domains in both DNA-bound and DNA-free states allow for efficient regulation. The model is likely relevant for many transcription factor systems, explaining the functional advantage of carrying sequentially close activation domains.

Graphical abstract

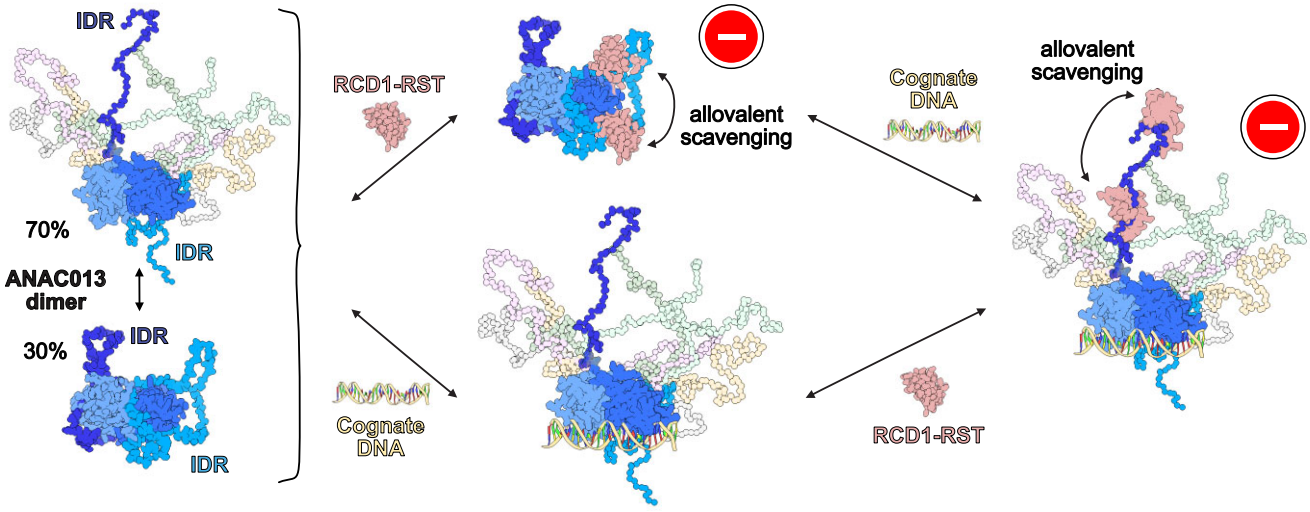

Received: April 17, 2024. **Revised:** January 18, 2025. **Editorial Decision:** January 20, 2025. **Accepted:** January 23, 2025

Introduction

Transcriptional programs regulate diverse biological processes such as stress responses and development, and they culminate in regulation of gene expression by gene-specific transcription factors. These consist of at least a DNA-binding domain (DBD) and an intrinsically disordered region (IDR), typically harboring the transcriptional activation domains (ADs) [1]. Due to their high content of intrinsic disorder (ID) [2, 3], ADs in transcription factors have been challenging to study. However, recent high-throughput studies have advanced the understanding of these functional units [4–6], for which ID properties and sequence features enable dynamic interactions, which are central to both coregulator interactions and the formation of regulatory condensates [7, 8]. Despite the vast information now available on the position and specific sequence features of ADs provided by these high-throughput studies, mechanistic insight into the details of regulation of AD interactions is still critically lacking.

So far, most structure–function studies of transcription factors have focused on their separate domains, ignoring intramolecular communication between order and disorder shown in some systems to be functionally important. For the tumor suppressor p53, the AD within the N-terminal IDR inhibits binding to nonspecific DNA through dynamic interactions with its DBD [9, 10], and phosphorylation in the IDR increases its affinity for the DBD, resulting in autoinhibition of promoter binding [11]. Conversely, in the SOX2 transcription factor, the C-terminal IDR interacts loosely and electrostatically with the DBD in an ensemble that is redistributed upon DNA binding to promote higher accessibility to one of the ADs [12]. These examples reveal intriguing yet incompletely understood ID-based regulation of transcription factor function, and studies addressing the role of interdomain communication in transcription factors are needed to enable mechanistic decomposition. Due to their simple structure with a single DBD and a single, but long C-terminal IDR, the plant-specific NAC [NAM (no apical meristem), ATAF (*Arabidopsis thaliana* activating factor), CUC (cup-shaped cotyledon)] transcription factors represent ideal molecular models for such studies [13].

The *A. thaliana* NAC transcription factor ANAC013 [also known as NTL1 (NAC with transmembrane motif 1-like 1)] is a regulator of oxidative stress responses [14] as well as of seed germination [15] in plants. As part of the mitochondrial retrograde regulation, reactive oxygen species (ROSs) elicit release of ER-membrane-bound ANAC013, which then translocates to the nucleus. Here, ANAC013 induces expression of target genes by binding to *cis*-regulatory elements in the UP-REGULATED BY OXIDATIVE STRESS (UPOX) promoter, enhancing oxidative stress tolerance [14]. The activity of ANAC013 is suppressed by interactions with Radical-induced Cell Death1 (RCD1) in coordination with ROS signals emitted from both mitochondria and chloroplasts [16]. RCD1 itself plays multiple roles in development and responses to ROS [17, 18]. It is a member of the αα-hub family of transcriptional regulators [19, 20] and uses its small helical αα-hub RCD–SRO–TAF4 (RST) domain for short linear motif (SLiM)-based interactions with ANAC013 and other transcription factors [21]. In ANAC013, the long C-terminal IDR encompasses the RCD1-interaction-SLiM (RIM) [21] and a transmembrane helix for ER-anchoring [14] (Fig. 1A).

NAC transcription factors have IDRs that differ in length with some up to hundreds of residues long and containing transcriptional ADs (see [21, 22]). A recent comprehensive work mapped ADs in the plant transcription factor proteome, revealing that some ADs exist alone in a long IDR and some ADs exist together with other ADs separated by linkers of various lengths [6]. Most of the ADs in plants have an unresolved interactome, although for some transcription factors, such as DREB2A, which carries two ADs, a few interactors are known. For DREB2A, this includes the negative regulator RCD1 that also binds to ANAC013, and the coactivator Med25 [23]. A splice variant where one of the ADs is missing exists for DREB2A [23, 24] and this provides tuning of transcriptional activation and abolishment of the negative regulation. Thus, the almost omnipresent IDRs of the transcription factors carry one or more ADs and play regulatory roles in transcription, highlighting the need for deeper mechanistic understanding of these IDRs for decoding transcriptional regulation.

Here, we address the molecular communication within ANAC013 and how binding of DNA and RCD1-RST affects this. From a high-throughput yeast-based assay, we identify three ADs in the IDR. Using biophysical methods, two acidic islands (AIs) in the IDR are shown to form localized and dynamic interactions with the DBD. These islands overlap with the ADs and are released from the DBD upon binding of both target promoter and nonspecific DNA. Intriguingly, interaction with the hub-domain RST of RCD1 is independent of DNA binding, just as DNA binding is independent of RCD1-RST binding. Through allovalency, RCD1-RST dynamically occupies the ADs at enhanced affinity. We propose an allovalency model for transcriptional regulation, where spatially close ADs are dynamically scavenged by the negative regulator in both free and DNA-bound states. The model is relevant for the functional understanding of the many other transcription factors currently appearing from high-throughput studies to carry closely spaced ADs.

Materials and methods

Protein expression and purification

The sequences coding for ANAC013 corresponding to residues M1–T274, S161–T274, S204–T234, and S161–G498 (UniProt F4EID2) were ordered from Twist Bioscience (San Francisco, CA, USA) and inserted into a modified pET-24b vector with an N-terminal 6xHis tag followed by SUMO. *Escherichia coli* NiCo21(DE3) cells (New England Biolabs) were transformed with one of the ANAC013 constructs and grown in lysogeny broth (LB) medium at 37°C until the optical density (OD) at 600 nm reached 0.6–0.8. Protein expression was induced either through autoinduction [25] or, when labeling for nuclear magnetic resonance (NMR), by addition of β-D-thiogalactopyranoside (IPTG) to a final concentration of 1 mM. The cultures were grown while shaking overnight at 18°C, and the cells were harvested by centrifugation. $^{15}N/^{13}C$- and ^{15}N-labeled samples were produced by growing transformed *E. coli* NiCo21(DE3) cells according to the protocol described previously [26]. For all productions, cells were resuspended in purification buffer [50 mM sodium phosphate, pH 8.0, 150 mM NaCl, 5 mM β-mercaptoethanol (BME)] supplemented with protease inhibitors (cOmplete EDTA-free, Roche Diagnostics) and were

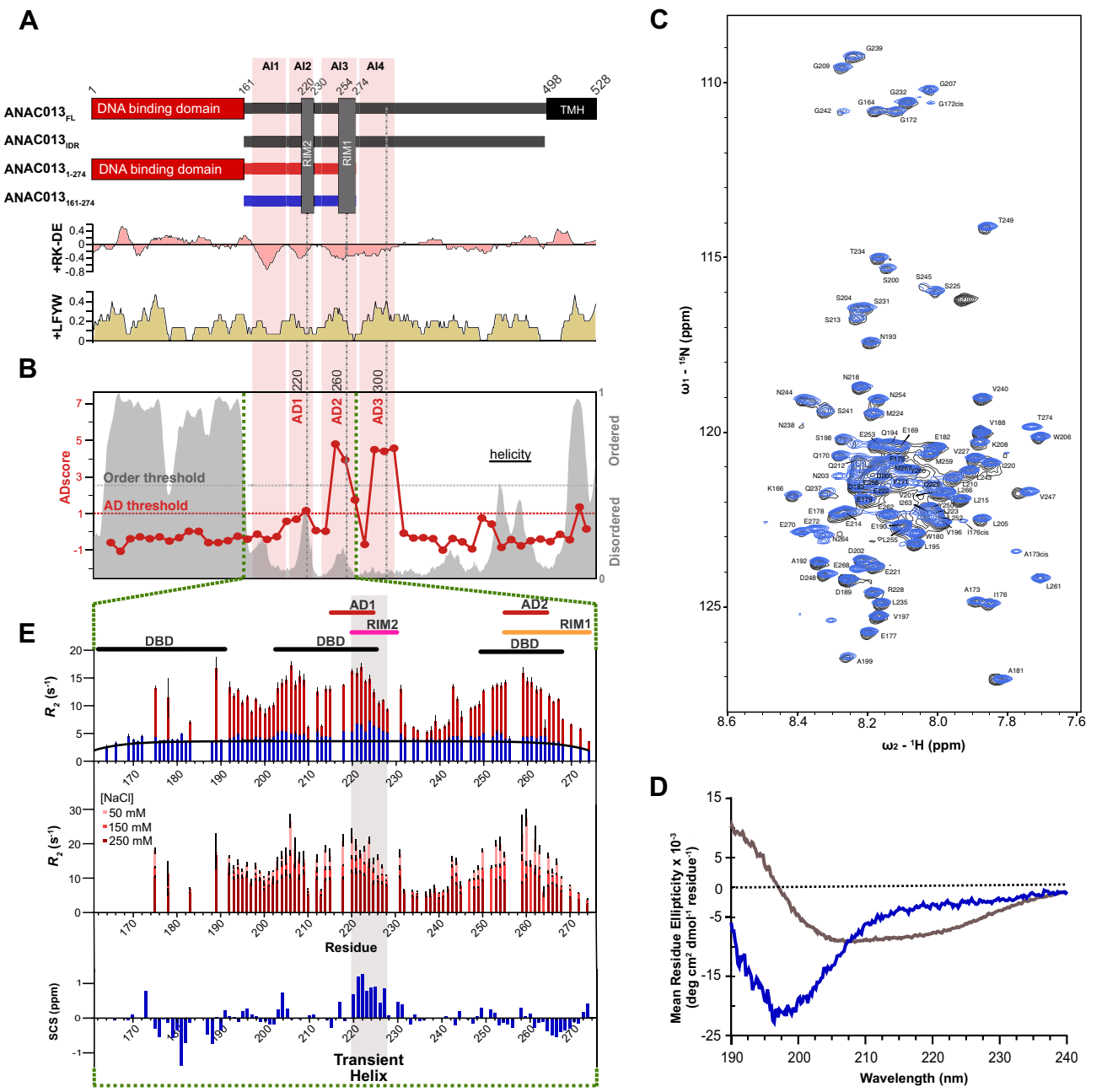

Figure 1. The IDR of ANAC013 interacts with its DBD through electrostatic interactions. (**A**) Schematic representation of ANAC013 and variants used in this study. TMH, transmembrane helix; RIM1 and RIM2, RCD1-RST interaction motifs, previously reported and identified here, respectively. AI, acidic islands. Lower panel: Charge distribution and L, F, Y, and W abundance in ANAC013 calculated by IDDomainSpotter [49]. (**B**) Disorder prediction (gray) (DISOPRED) [72] in ANAC013 and AD scores (red) of 40 residue tiles as a function of the tile center position. (**C**) ^{1}H, ^{15}N HSQC (Heteronuclear Single Quantum Coherence) spectrum of ANAC013$_{161–498}$ (gray) and of the assigned ANAC013$_{161–274}$ (blue). (**D**) Far-ultraviolet (far-UV) circular dichroism (CD) spectrum of ANAC013$_{161–498}$ (gray) and of ANAC013$_{161–274}$ (blue). (**E**) Top panel: Transverse relaxation rates (R_2), obtained for ANAC013$_{1–274}$ (red) and ANAC013$_{161–274}$ (blue). Black line corresponds to random coil R_2 values [35]. Middle panel: R_2 values for ANAC013$_{1–274}$ at different NaCl concentrations. All relaxation rates were obtained at 10°C and a ^{1}H frequency of 750 MHz. Lower panel: SCS of C$^{\alpha}$ of ANAC013$_{161–274}$.

disrupted by eight French press (Constant Systems, Daventry, UK) cycles at 25 kpsi. The extract was centrifuged at 20 000 × *g* for 45 min at 4°C.

ANAC013$_{204–234}$ was purified on a gravity flow Ni Sepharose 6 fast flow column (Cytiva) followed by size-exclusion chromatography (SEC). After a washing step with a purification buffer containing 20 mM imidazole, the protein was eluted with purification buffer containing 250 mM imidazole. The obtained protein fraction was dialyzed against purification buffer and digested overnight at 4°C by ULP1 produced as described [27]. After removal of His$_6$-SUMO by a second gravity flow Ni Sepharose 6 fast flow column (Cytiva), SEC was performed on a Superdex 75 10/300 column (GE Healthcare) equilibrated with NMR buffer [20 mM sodium phosphate, pH 7.4, 150 mM NaCl, 2 mM dithiothreitol (DTT)]. ANAC013$_{161–274}$ was purified using a similar protocol, except for an additional anion exchange chromatography (MonoQ, GE Healthcare) step between the second Ni^{2+}

affinity column and the SEC. The protein was loaded onto the MonoQ column in 20 mM sodium phosphate, (pH 8.0), 150 mM NaCl, and 5 mM BME, and was eluted using a NaCl gradient to 1 M NaCl. ANAC013$_{1–274}$ was purified using the same protocol as ANAC013$_{161–274}$ without the second Ni^{2+} affinity column. The SEC was performed using a Superdex S200 10/300 column (GE Healthcare) in NMR buffer.

Cells expressing ANAC013$_{161–498}$ were lysed in 50 mM sodium phosphate, (pH 6.0), 150 mM NaCl, 6 M urea, and 5 mM BME. After centrifugation, the supernatant was applied to a HiTrap Q FF 5 ml column (GE Healthcare) and eluted using a 20 mM to 1 M NaCl gradient. Fractions containing ANAC013$_{161–498}$ were pooled and dialyzed against 20 mM sodium phosphate (pH 8.0), 150 mM NaCl, 5 mM BME at 4°C. After 1 h, the dialysis bath was changed, and ULP1 was added to the dialysis bag overnight. The sample was then applied to a gravity flow Ni Sepharose 6 fast flow column (Cytiva) equilibrated in dialysis buffer. The flow-through was further purified using SEC with a Superdex S200 column 10/300 (GE Healthcare) equilibrated in the NMR buffer. ANAC013 RIM1 corresponding to residues 254–274 (UniProt F4EID2) and the RCD1-RST domain (residues 499–572) (Uniprot M5BF30), were expressed and purified as previously described [28, 29]. The purity and monodispersity of all samples were checked by sodium dodecyl sulfate–polyacrylamide gel electrophoresis, dynamic light scattering, and mass spectrometry.

High-throughput screening for ADs in the *A. thaliana* transcription factor ANAC013

The ANAC013 protein sequence was divided into 40 amino acid residue tiles with a step size of 10 amino acid residues. Yeast codon-optimized sequences for each ANAC013 tile were synthesized and cloned in bulk into pMVS1421 [4] creating synthetic transcription factors consisting of an N-terminal mCherry tag, a mouse Zif269 DBD, an estrogen binding domain, and the tested ANAC013 tile expressed under the yeast actin 1 (ACT1) promoter as described [4]. The expression cassette was cloned into the mating type A strain DHY211 (courtesy of Angela Chu and Joe Horecka) using homologous recombination at the URA3 locus as previously described [4]. Positive strains carrying the synthetic transcription factor were mated to yeast carrying a GFP reporter driven under the P3 promoter. Yeast were sorted based on reporter to transcription factor ratio (GFP:mCherry), and each bin was sequenced to determine the abundance of each fragment tested. A corresponding AD score was calculated by taking the dot product of fragment abundance in each bin by the median GFP:mCherry ratio of each bin. Activity of synthetic control transcription factors with known ADs is shown in Supplementary Fig. S1A [6].

NMR measurements

All samples for NMR contained 20 mM sodium phosphate (pH 7.4), 150 mM NaCl, 2 mM DTT, 10% (v/v) D_2O, and 2 mM DSS. The assignment of ANAC013$_{161–274}$ was obtained using a set of BEST-TROSY-type experiments [30] recorded at 10°C using a ^{15}N, ^{13}C-labeled sample (370 μM) using a Bruker spectrometer operating at a ^{1}H frequency of 750 MHz, equipped with a cryoprobe. A small number of weak resonances from proline *cis*/*trans* isomers around P174 were observed. The assignment of the RCD1-RST domain bound to ANAC013$_{161–274}$ was obtained at 20°C using a ^{15}N, ^{13}C-labeled sample containing unlabeled ANAC013$_{161–274}$ at a equimolar ratio (200 μM of each protein) using BEST-TROSY-type triple-resonance experiments [30] and 20% nonuniform sampling [31] on the same spectrometer. The spectra were processed using qMDD [32], manually peak-picked in POKY [33], and MARS [34] was used for identification of spin systems followed by manual verification. The obtained assignments were then transferred to 10°C using HSQCs recorded every 2.5°C.

For the NMR relaxation data, the following protein concentrations were used: 370 μM for ANAC013$_{161–274}$, 140 μM for ANAC013$_{1–274}$, and 108 μM for ANAC013$_{1–274}$ salt titration; 100 and 80 μM equimolar admixtures for ANAC013$_{1–274}$:proUPOX and ANAC013$_{1–274}$:scrUPOX, respectively; and 80 μM equimolar admixture for ANAC013$_{1–274}$:proUPOX:RST. Measurements of ^{15}N transverse relaxation rates of ANAC013$_{1–274}$, ANAC013$_{161–274}$, ANAC013$_{1–274}$:DNA, and ANAC013$_{1–274}$:DNA:RCD1-RST were obtained at 10°C on a Bruker spectrometer operating at a ^{1}H frequency of 750 MHz with a cryoprobe. The magnetization decay was sampled at 16.96, 33.92, 50.88, 101.76, 135.68, 203.52, 237.44, 271.36, 407.04, and 542.72 ms. All spectra were processed in qMDD [32], peak heights were extracted using POKY [33], and relaxation rates were calculated using Prism fitting to a single exponential decay function. Random coil R_2 values were calculated according to the following equation, where R_{int} is the intrinsic relaxation rate set to 0.27 s^{-1}, λ_0 is the persistence length of the polypeptide chain set to 7, and N is the total length of the polypeptide [35]:

$$R_2^{rc}(i) = R_{int} \sum_{j=1}^{N} e^{\frac{|i-j|}{\lambda_0}}.$$

NMR peak intensity ratios for ANAC013$_{1–274}$:DNA and ANAC013$_{1–274}$:DNA:RCD1-RST were extracted from standard HSQC-type pulse sequences from Bruker BioPack, which were recorded along with the relaxation measurements.

Titration experiments of ^{15}N ANAC013$_{1–274}$ and ^{15}N ANAC013$_{161–274}$ with RCD1-RST were recorded on a 50 μM sample where RCD1-RST was added at molar ratios varying from 0.5 to 2 at 10°C on a Bruker spectrometer operating at a ^{1}H frequency of 800 MHz with a cryoprobe using standard HSQC-type pulse sequences from Bruker BioPack. Interactions of ^{15}N RCD1-RST with ANAC013$_{161–274}$, ANAC013$_{254–274}$, or ANAC013$_{204–234}$ were recorded on a 50 μM sample where ANAC013 was added at a 1:1 (ANAC013$_{161–274}$ and ANAC013$_{254–274}$) or 4:1 (ANAC013$_{204–234}$) ratio and were obtained at 10°C on a Bruker spectrometer operating at a ^{1}H frequency of 750 MHz (ANAC013$_{161–274}$ and ANAC013$_{254–274}$) or 600 MHz (ANAC013$_{204–234}$) using standard HSQC-type pulse sequences from Bruker BioPack. The titration of ANAC013$_{204–234}$ with RCD1-RST was done with 100 μM ANAC013 on a 750 MHz instrument at 10°C with RCD1-RST concentration from 0 to 4 molar equivalents.

Chemical shift perturbations from titration experiments

Perturbations of amide chemical shifts, also termed chemical shift perturbations (CSPs), comparing the chemical shifts in the absence and presence of varying concentrations of binding

partner, were calculated using the following equation:

$$\mathrm{CSP} = \sqrt{(\Delta\delta_{\mathrm{H}}{}^2) + (0.154 * \Delta\delta_{\mathrm{N}}{}^2)},$$

where 0.154 is a scaling factor based on the relative average standard deviations of H^N and N nuclei in proteins [36]. Secondary chemical shifts (SCSs) of C^α, C^β, and C chemical shift values were obtained using random coil referencing [37, 38] and calculated as follows:

$$\mathrm{SCS} = \Delta\delta = \delta_{\mathrm{observed}} - \delta_{\mathrm{random\ coil}}.$$

CD spectropolarimetry

Far-UV CD measurements were performed on a Jasco J-810 spectropolarimeter equipped with a Peltier-controlled cuvette holder in a 1 mm path-length quartz cuvette (HELMA). A protein sample of 2.7 μM was prepared in 10 mM Na_2HPO_4/NaH_2PO_4 (pH 7.4), 137 mM NaF, and 0.5 mM TCEP (tris(2-carboxyethyl)phosphine). The spectrum was recorded at 10°C from 260 to 190 nm, data pitch was 0.1 nm, digital integration time was 2 s, and the measurement was performed with a scan speed of 10 nm/min for 10 accumulations. The high-tension voltage was kept below 700 V during all accumulations. Identical settings were used to record a buffer spectrum for subtraction. Data were converted to mean residue ellipticity (θ_{MRE}) using the following equation:

$$\theta_{\mathrm{MRE}} = \frac{\theta}{10 \times c \times l \times n}$$

where θ is the measured intensity in mdeg, c is the molar protein concentration, l is the path length in cm, and n is the number of peptide bonds in the protein.

Small angle X-ray scattering of $ANAC013_{1–274}$ and $ANAC013_{161–274}$

SEC–small angle X-ray scattering (SAXS) experiments of $ANAC013_{161–274}$ and $ANAC013_{1–274}$were obtained at 20°C at the P12 EMBL BioSAXS beamline [39], at PETRA III, EMBL Hamburg, which operated at a fixed energy (10 keV, λ = 0.123981 nm). The associated SEC–MALLS (size exclusion-magic angle laser light scattering) was carried out using a Superdex S200 increase 10/300 column (GE Healthcare) at a flow rate of 0.65 ml min^{-1} with an injection volume of 70 μl and a running buffer composed of 20 mM HEPES (pH 7.4), 150 mM NaCl, 5 mM $NaNO_3$, and 5 mM TCEP. Frames were each 1 s in duration using the Pilatus 6M detector (Dectris) placed 3 m from the sample. Samples were purified as described above and consisted of $ANAC013_{161–274}$ (70 μl, 9.1 mg ml^{-1}) and $ANAC013_{1–274}$ (70 μl, 8.6 mg ml^{-1}). SEC–MALLS data analysis was carried out using the ASTRA7 software. SAXS data were processed using the ATSAS package [40]. To analyze the experimental SAXS data of $ANAC013_{161–274}$, a 20 000-structures ensemble was generated using flexible-meccano [41, 42], using the secondary structure propensities previously determined as input (20% helix for residues 220–228). The theoretical SAXS curves of each structure from the ensemble were predicted using CRYSOL [43] and averaged to represent the ensemble and compared to experimental data using CRYSOL [43]. The five best-fitting structures from the ensemble were selected, their SAXS curves averaged, and compared to experimental data. To analyze the experimental SAXS data of $ANAC013_{1–274}$, two states were considered. A closed form, where the IDR interacts with the positively charged islands of ANAC013 DBD, was generated. To do this, the structure model of the DBD dimer was predicted using AlphaFold2 [44], and manual sculpting in PyMOL using experimentally determined contact areas to generate the final structure. An open form was generated using the DBD dimer model predicted by AlphaFold2 and flexible-meccano was employed to add the flexible IDR to the predicted structure, assuming statistical coil distribution for these amino acids (residues 183–274). SAXS curves were predicted for each form ("closed" structure and "open" ensemble) by averaging predicted SAXS curves for individual structures over the entire ensemble using CRYSOL [43]. The two predicted SAXS curves were then combined in a population-weighted average to best describe the experimental data using OLIGOMER [45].

Isothermal titration calorimetry

All isothermal titration calorimetry (ITC) experiments were performed on either a MicroCal ITC200 or a Malvern Panalytical PEAQ-ITC at 25°C. Experiments were performed using 1 + 13–18 injections of 0.5 and 2–3 μl with delays of 150 s or longer and a stirring speed of 750 rpm. Before the experiments, ANAC013 and RCD1-RST were dialyzed into ITC buffer (20 mM sodium phosphate, pH 7.4, 150 mM NaCl) and degassed by centrifugation at 20 000 × g for 20 min at the experimental temperature. For ANAC013 fragments containing cysteine residues, proteins were dialyzed into ITC buffer containing 2 mM DTT. Interaction of RCD1-RST with $ANAC013_{1–274}$:proUPOX was done in duplicate. All other experiments were done in triplicates. Supplementary Table S2 provides details of each experiment. All binding isotherms were analyzed by a nonlinear least-squares fit of the experimental data to a single site model, or the two sets of sites model as described by Microcal. Reported K_D errors are asymmetric, and confidence intervals should be determined from the free energy standard deviation.

Simulation of ITC experiments

ITC experiments of ANAC013 RIM2–RIM1 fragments were simulated using a COPASI setup by performing time course simulations with an event trigger that would "inject" a certain amount of protein into a cell volume. An equilibration time of 60 s between injections was used. Interaction rate constants were arbitrarily selected to yield the desired dissociation constants. Diffusion rates involved in the allovalent model were assumed similar to the values used by Klein *et al.* [46]. Displaced volume from injections was not considered and simulated enthalpy was calculated from the change in concentration of the involved species based on concentrations extracted immediately before and 50 s after each simulated injection. Simulated injection error bars represent standard deviations of 100 simulations using parameters sampled from the experimental parameter distributions.

Results

The ANAC013 IDR contains three ADs and forms soluble oligomers

Like in our previous work [23], we used a high-throughput yeast-based assay to screen the entire sequence of ANAC013

for ADs using 40-residue tiles (Fig. 1B and Supplementary Fig. S1A) [6]. Based on synthetic transcription factors containing a DBD targeting a GFP reporter gene, an mCherry fluorescence tag for quantification, and a variable putative AD from the ANAC013 sequence, the transcriptional activity was taken by proxy of the AD score of each tile calculated from the fluorescence intensity ratio of GFP to mCherry. The screen identified three ADs in ANAC013 (Fig. 1B). Although AD1 (centered around residue 220) scored just above the set threshold, it was retained in our further analysis as this region contains a previously reported EDLL-like activation motif (residues 214–227) [47]. AD2 overlapped with the previously identified RIM [21], and AD3 was located C-terminally to AD2, centered around residue 300 (Fig. 1B). Since ADs are often enriched in acidic residues balanced by leucines and aromatic residues [48, 49], we mapped the charge patterning and leucine and aromatic abundance in ANAC013 using IDDomainSpotter [49], (Fig. 1A, lower panel). Four stretches carried an excess negative charge; hence, we will refer to these as acidic islands (AI1–AI4, Fig. 1A). Strikingly, AI2 coincided with AD1, AI3 with AD2, and AI4 with AD3, and all were associated with a high degree of hydrophobicity, with AI4 being the most hydrophobic. Thus, the ANAC013 ADs fall into the category of acidic ADs with leucines and aromatics (Fig. 1A, lower panel), and we refer to these regions as AD1/AI2, AD2/AI3, and AD3/AI4. AI1 lacks the accompanying hydrophobicity and does not coincide with an AD.

To investigate the behavior of intra- and intermolecular interactions within ANAC013 (Fig. 1A), we excluded the transmembrane helix and focused on the ANAC013 IDR (residues 161–498), containing the three ADs. Using NMR spectroscopy, only ∼100 of the expected 321 NMR resonances were observed in the ^{1}H, ^{15}N HSQC NMR spectrum, located within a narrow ^{1}H dispersion typical of IDRs (Fig. 1C). A SEC analysis indicated higher order soluble structures (Supplementary Fig. S1B), and a far-UV CD spectrum revealed the presence of ∼15% helicity (Fig. 1D), in line with PSIPRED prediction of helicity in the regions 420–460 (Supplementary Fig. S1C). Furthermore, predictors of phase separation reported a high score of 0.78 (PSPredict) [50] and predicted two ∼20-residue stretches outside the ADs centered around F280 and M510 with propensity for driving phase separation (ParSe) [51]. Thus, the ANAC013 IDR has a propensity to form intermolecular interactions. We therefore assessed whether supramolecular interactions could explain the lack of NMR signals and recorded a ^{1}H, ^{15}N HSQC spectrum of ANAC013$_{161–498}$ in 6 M urea (Supplementary Fig. S1D). All resonances were recovered, indicating that a relatively large part (∼2/3) of the ANAC013 IDR contributes to these structures.

Based on these results, we produced a shorter fragment, ANAC013$_{161–274}$ (Fig. 1A), corresponding to the N-terminal 1/3 of the IDR and comprising AI1, AD1/AI2, and AD2/AI3, the latter including the RIM (residues 254–274) [21, 24]. The ^{1}H, ^{15}N HSQC spectrum of ANAC013$_{161–274}$ overlapped nearly perfectly with that of ANAC013$_{161–498}$ at native conditions (Fig. 1C), demonstrating that the inferred internal associations involve residues ∼280–498, obscuring access to this region as well as to AD3/AI4 directly. As ANAC013$_{161–274}$ constitutes a functional hot spot, containing two of the ADs and the previously identified biologically relevant coregulator binding site, RIM, we focused on this region of ANAC013.

The ANAC013 IDR interacts with the DBD through negatively charged islands—AIs

Using a set of BEST-type triple-resonance NMR experiments, we assigned the backbone resonances of ANAC013$_{161–274}$ to 81% completeness (Fig. 1C and E; BMRB: 51969). The secondary $^{13}C^{\alpha}$ and $^{13}C^{\beta}$ chemical shifts (Fig. 1E and Supplementary Fig. S2) showed few consistent patterns from transient secondary structures, inferring that ANAC013$_{161–274}$ is mostly disordered, except for a transient helix between D217 and G232. This helix is populated to ∼20% as deduced from consecutive positive SCSs [52] and overlaps AD1/AI2 (Fig. 1E). The dominant disorder was confirmed by a minimum at 200 nm in the far-UV CD spectrum (Fig. 1D). We measured ^{15}N transverse relaxation rates (R_2) and compared these to calculated R_2 rates of random coil behavior [35] (Fig. 1E, upper panel). Significantly elevated R_2 values were observed for N218–S231, consistent with the existence of a transiently populated helix.

To investigate the effect of the DBD on the IDR behavior, we produced and purified ANAC013$_{1–274}$ (Fig. 1A), which, as expected [30], was dimeric as confirmed by SEC–MALLS analyses (Supplementary Fig. S3). Its visible resonances in the ^{1}H, ^{15}N HSQC spectrum overlapped nearly perfectly with those of ANAC013$_{161–274}$ (Supplementary Fig. S4), allowing transfer of assignments. Compared to ANAC013$_{161–274}$, we observed line broadening to different degrees. Resonances corresponding to all residues up to V188 were broadened beyond detection, suggesting these either belong to the folded DBD dimer—itself not visible due to its large size (43 kDa)—or interact with the DBD on an intermediate NMR timescale. We measured R_2 rates and compared those to the R_2 values for the IDR alone (ANAC013$_{161–274}$) (Fig. 1E, upper panel). Generally, an increase in the R_2values was seen across the IDR, suggesting slower tumbling rates when fused to DBD. Larger increases were concentrated to three regions. The first region is directly connected to the DBD, where R_2values from D189–S200 gradually decreased, suggesting that residues up to D185 would be part of the folded DBD. To address this hypothesis, we used AlphaFold2 [44] to predict the model structure of the ANAC013 dimer (ANAC013$_{1–274}$) alone and in the presence of UPOX DNA, a previously identified target promoter *cis*-element [14]. We observed that residues S161 to D183, which overlap AI1, fold onto the DBD in *trans* (Supplementary Fig. S5A). AI1 contacts the DBD outside the DNA binding region, especially around a basic β-strand-connecting loop (62-KTRDR-66). AI1 forms an α-helix and its binding in *trans* helps orient a loop region (residues 162–166) that binds to the minor groove of DNA (Supplementary Fig. S5B). The model structures of ANAC013 were found to be almost identical in the absence and presence of UPOX DNA ($RMSD_{C\alpha}$ = 0.51 Å), supporting the hypothesis that residues S161 to D183 are indeed part of the folded DBD. The two other regions with increased R_2values were S200–Q230, AD1/AI2, comprising the transient helix, and V240–E270, AD2/AI3, comprising the RIM (Fig. 1A). The DBD is overall positively charged, with several charged patches, mostly in the DNA binding surface [53, 54], but also on the side opposite to it [54] (Supplementary Fig. S5C and D). We therefore hypothesized that the IDR interacts with the DBD through dynamic electrostatic interactions between negatively (IDR) and positively (DBD) charged areas. Indeed, R_2 rates showed a gradual decrease across the IDR with increasing ionic strength

(Fig. 1E, middle panel), reflecting screening of the DBD–IDR interaction involving the AD1/AI2 and AD2/AI3 and confirming the observed interactions to be mainly electrostatic.

ANAC013 DBD–IDR exists in an open and closed state equilibrium

To obtain a representation of the overall structural properties of ANAC013$_{161–274}$ and ANAC013$_{1–274}$, both were investigated using SEC–SAXS. To analyze the SAXS profile for ANAC013$_{161–274}$, flexible-meccano, a statistical coil generator [41, 42], was used to generate 20 000 conformers, and a SAXS curve predicted for each one. The average SAXS curve of these conformers did not reproduce the experimental data accurately ($\chi^2 = 25$) (Supplementary Fig. S6A), indicating that ANAC013$_{161–274}$ does not behave as a statistical coil. The average R_g of this ensemble (31 Å) was smaller than the experimentally determined R_g (36 Å) (Supplementary Fig. S6B), showing ANAC013$_{161–274}$ to be extended in solution, consistent with its net negative charge (Fig. 1A, middle panel), and correlating with the R_2 values that were overall higher than expected for a random coil (Fig. 1D). The conformers were then ranked by their ability to reproduce the experimental SAXS curve and the five best conformations chosen to represent the ensemble structure of ANAC013$_{161–274}$ (Fig. 2A and Supplementary Fig. S6C). The average SAXS curve of these expanded conformers reproduced the experimental data well ($\chi^2 = 1.08$), consistent with repulsion between the three AIs. The transient helix (D217–G232) was partially populated in this ensemble (one out of five conformers, 20%), consistent with the SCSs from NMR.

For ANAC013$_{1–274}$, we generated a flexible-meccano ensemble of 10 000 conformers [41, 42], where the IDR could explore all the available conformational space and modeled the observed interaction between the DBD and the IDR using a combination of AlphaFold2 and manual sculpting. We then used OLIGOMER [45] to approach the experimental SAXS data using a weighted average of the ensemble with the IDR both in an open state and in the modeled closed state where AD1/AI2 and AD2/AI3 interact with the DBD (Fig. 2B and Supplementary Fig. S7). Despite the crudeness of the model, the obtained average SAXS curve represented the experimental data well ($\chi^2 = 2.53$) and showed that ANAC013$_{1–274}$ in solution is in equilibrium between ∼30% (31%) closed and ∼70% (69%) open forms. The obtained χ^2 also suggested the presence of other minor species unaccounted for in the model, such as single AIs bound to the DBD. These were not considered further.

DNA binding shifts the equilibrium toward the open state by releasing the IDR from the DBD

To investigate whether and how the interaction between the ANAC013 IDR and the DBD would influence DNA binding and vice versa, we used the two different ANAC013 fragments: the DBD alone (ANAC013$_{1–183}$) and the DBD with the IDR (ANAC013$_{1–274}$). We chose a previously identified target promoter *cis*-element proUPOX [14], as well as a scrambled DNA of that sequence, scrUPOX, serving as a nonspecific DNA control (Supplementary Table S1). The thermodynamic parameters of the interaction were determined by ITC (Table 1 and Fig. 2C). The dissociation constants K_D of the complexes with proUPOX were similar, with $K_D = 438 \pm 13$ and 550 ± 110 nM for ANAC013$_{1–183}$ and ANAC013$_{1–274}$, respectively. A stoichiometry of 1:2 (DNA to ANAC013 monomer) was found, consistent with a previously determined structure of a DNA-bound DBD from the NAC family [53,54]. Strikingly, proUPOX interaction with ANAC013$_{1–274}$ displayed a much smaller entropic penalty compared to ANAC013$_{1–183}$:proUPOX, with the entropy difference between the free and bound states $-T\Delta S$ of 9 and 32 kJ mol^{-1}, respectively (Table 1). This suggests that the longer IDR contributes with favorable conformational entropy in DNA binding and that there is enthalpy–entropy compensation [55]. At the same conditions, binding could not be detected for any of the variants using the scrUPOX control DNA (Supplementary Fig. S8).

To understand this entropic driving force, we investigated the behavior of the IDR upon DNA binding using NMR and added stoichiometric amounts of proUPOX to the ^{15}N-labeled ANAC013$_{1–274}$ dimer. Peak intensities corresponding to residues from AD1/AI2 and AD2/AI3 increased, suggesting a DNA-driven increase in dynamics in accordance with the ITC data (Table 1), and hence a release of the IDR from the DBD (Supplementary Fig. S9). This was also recapitulated in reduced R_2values of the IDR for ANAC013$_{1–274}$:proUPOX compared to free ANAC013$_{1–274}$ caused by increased dynamics (Fig. 2D). Interestingly, adding scrUPOX yielded similar results (Fig. 2D), suggesting that even nonspecific DNA can release the IDR from the DBD, despite a lack of measurable binding to the ANAC013-DBD by ITC.

Simultaneous DNA and coregulator binding

RCD1 downregulates the expression of ANAC013 target genes [16]. Using ITC, we confirmed that RCD1-RST is able to form a 1:1 complex with ANAC013$_{1–274}$ when titrated into a prebound ANAC013$_{1–274}$:proUPOX complex. This interaction (K_D of 60 ± 1 nM) was mainly, but not only, driven by enthalpy ($\Delta H = -45 \pm 1$ kJ mol^{-1}) (Fig. 2C and Table 1). We then used NMR to assess whether RCD1-RST binding to ANAC013 could disrupt or prevent interaction with target DNA. Stoichiometric amounts of RCD1-RST to ANAC013 monomer were added to a preformed ^{15}N-labeled ANAC013$_{1–274}$:proUPOX complex. Upon addition of RCD1-RST, NMR intensity losses were observed in two regions of the IDR overlapping with, but not fully covering, AD1/AI2 and AD2/AI3 (Fig. 2E). Unexpectedly, RCD1-RST bound to DNA-loaded ANAC013 at not one, but two different sites. R_2 measurements confirmed that the IDR of ANAC013$_{1–274}$ remained flexible when bound to both RCD1-RST and DNA (Fig. 2F), but also suggested that RCD1-RST did not disrupt ANAC013 interaction with proUPOX. Vice versa, when adding proUPOX to a prebound ^{15}N-ANAC013$_{1–274}$:RCD1-RST complex, we observed NMR signal intensity increases from the release of the IDR from the DBD (Fig. 2G), as was the case for ANAC013$_{1–274}$ binding to proUPOX (Supplementary Fig. S9). Thus, binding of RST to ^{15}N-ANAC013$_{1–274}$ does not abolish the DBD:DNA interaction, or the IDR interaction with the DBD. Notably, comparing the NMR signal decreases in Fig. 2E with the regions that display high R_2values and interact with the DBD in Fig. 2D, it becomes clear that the DBD and the RST binding regions overlap but are not identical. This suggests that in the absence of DNA, the IDR retains its ability to bind to RCD1-RST while still contacting the DBD. This is also supported by the broader IDR regions involved in DBD binding compared to those involved

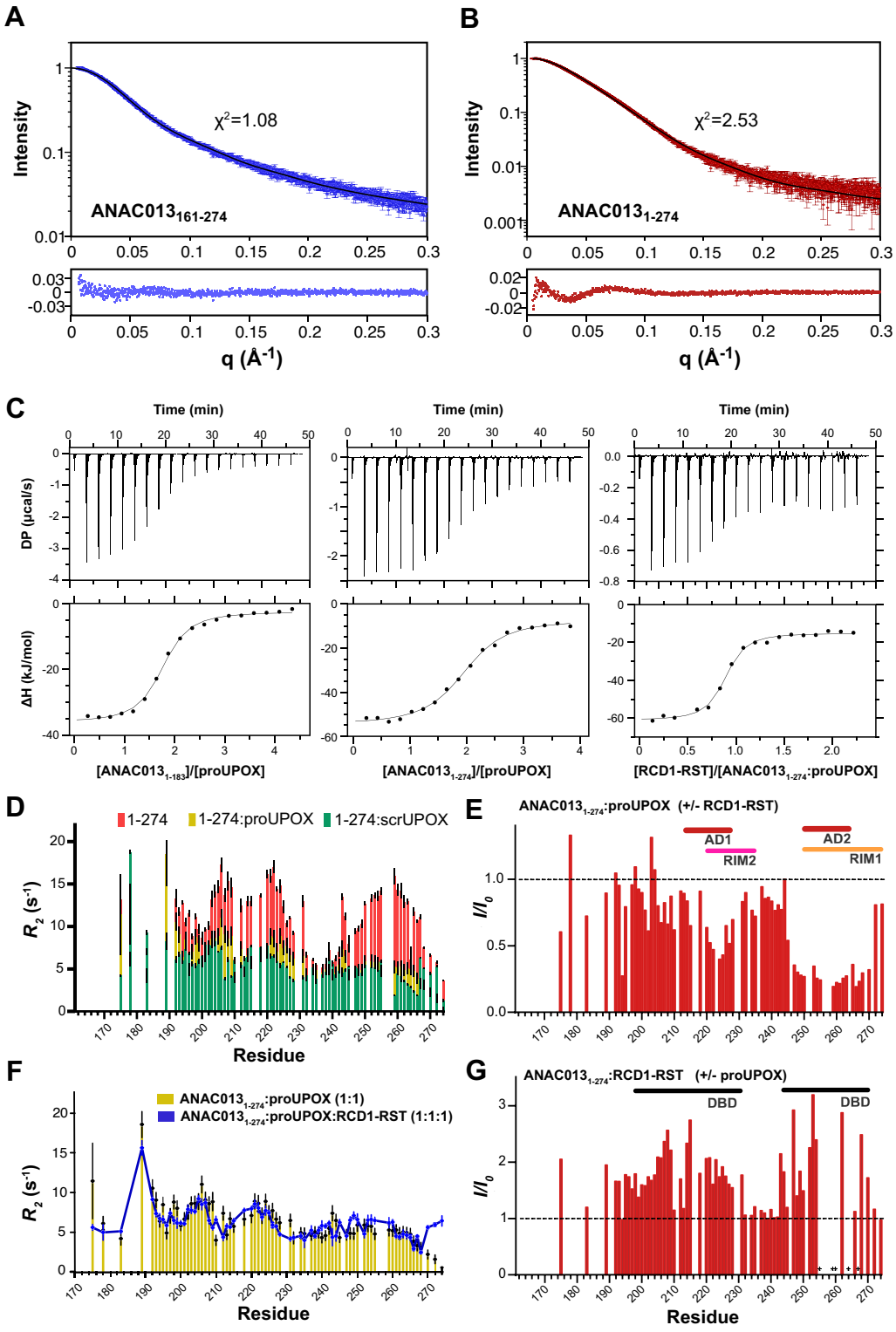

Figure 2. ANAC013 interacts simultaneously with DNA and RCD1-RST. (**A**) Experimental SAXS curve obtained in SEC–SAXS for ANAC013$_{161–274}$ (dark blue line) against the average theoretical SAXS curve of the ensemble of five conformers selected to represent the ANAC013$_{161–274}$ structure (black line). Residuals are shown below. (**B**) Experimental SAXS curve obtained in SEC–SAXS for ANAC013$_{1–274}$ (red) against the average theoretical SAXS curve obtained from the weighted average (black line) of the SAXS curves of an ensemble with a free IDR (open) and DBD-bound IDR (closed) model (∼70% and ∼30%, respectively, as determined by OLIGOMER). Residuals are shown below. (**C**) Representative ITC data of the interaction between ANAC013$_{1–183}$ (left) or ANAC013$_{1–274}$ (middle) and proUPOX DNA, and between RCD1-RST and ANAC013$_{1–274}$:proUPOX (right). (**D**) Transverse relaxation rates, R_2, for ANAC013$_{1–274}$ (red), ANAC013$_{1–274}$:proUPOX (curry), and ANAC013$_{1–274}$:scrUPOX (dark green). (**E**) HSQC intensity profile (I/I_0) of ANAC013$_{1–274}$:proUPOX:RCD1-RST 1:1:1 (I) compared to ANAC013$_{1–274}$:proUPOX 1:1 (I_0). (**F**) Transverse relaxation rates, R_2, for ANAC013$_{1–274}$:proUPOX (curry bars) and ANAC013$_{1–274}$:RCD1-RST:proUPOX 1:1:1 (dark blue line). (**G**) HSQC intensity profile (I/I_0) of ANAC013$_{1–274}$:RCD1-RST:proUPOX 1:1:1 (I) relative to ANAC013$_{1–274}$:RCD1-RST 1:1 (I_0). Black bars indicate the areas involved in intramolecular interaction of the IDR with the DBD. Stars indicate resonances recovered upon addition of proUPOX.

Table 1. Thermodynamic analyses of ANAC013 interactions with DNA in the presence and absence of RCD1-RST$_{499–572}$

Cell	Syringe	K_D (nM)	N	ΔH (kJ mol^{-1})	$-T\Delta S$ (kJ mol^{-1})	ΔG (kJ mol^{-1})
proUPOX	ANAC013$_{1–183}$	438 ± 13	1.70 ± 0.01	−68 ± 1	32	−36
proUPOX	ANAC013$_{1–274}$	547 ± 110	1.98 ± 0.05	−44 ± 2	9	−36
scrUPOX	ANAC013$_{1–183}$	No binding				
scrUPOX	ANAC013$_{1–274}$	No binding				
ANAC013$_{1–274}$:proUPOX[a]	RCD1-RST	60 ± 1	0.84 ± 0.01	−45 ± 1	4	−41

[a]ANAC013$_{1–274}$:proUPOX was in the cell to avoid dissociation of DNA upon injection.

in binding RCD1-RST (Fig. 2E and G). Taken together, these data showed that ANAC013$_{1–274}$ can bind cognate DNA even when already bound to RCD1-RST and vice versa, highlighting the ability of ANAC013 to simultaneously bind DNA and its negative regulator.

ANAC013 contains a second binding site for RCD1-RST

To decompose a possible second RCD1-RST binding site in ANAC013, we first re-established the interaction between the ANAC013-RIM (N254–T274) and RCD1-RST using ITC at the current conditions, showing the formation of a 1:1 complex with a K_D of 70 ± 30 nM (Table 2 and Fig. 3A, left panel) consistent with previous work (K_D = 9 ± 4 nM; different buffers [21]). We then explored the N-terminal context and followed the addition of RCD1-RST to ANAC013$_{1–274}$ or ANAC013$_{161–274}$ by NMR. ANAC013 resonances did not show measurable CSPs upon RCD1-RST addition but underwent extensive line broadening, suggesting slow exchange on the NMR timescale (Fig. 3B and Supplementary Fig. S10A). In both instances, residues corresponding to the RIM (N254–T274) located in AD2/AI3 were broadened beyond detection at a 1:1 ratio of RCD1-RST:ANAC013 (Fig. 3B and Supplementary Fig. S10B). However, a second interaction site was identified in ANAC013 between I220 and Q230, corresponding to the transient helix located in AD1/AI2 (Fig. 1E and Supplementary Fig. S2). For this second site, which bears sequence similarities to the known RIM (Supplementary Fig. S10C), resonances were broadened beyond detection at a ratio of RCD1-RST:ANAC013$_{161–274}$ of 1.5:1, suggesting a weaker affinity compared to RIM1 (Fig. 4B). We term this second site RIM2 (residues I220–Q230), keeping the known site (N254–T274) as RIM1 (Fig. 1A).

To investigate the RIM2 interaction with RCD1-RST separately, we produced ANAC013$_{204–234}$ and studied the interaction by ITC. This revealed a K_D of 11 ± 2 μM (Table 2 and Fig. 3A, middle panel). The large entropic penalty ($-T\Delta S$ = 25 ± 5 kJ mol^{-1}) as well as large enthalpy contribution (ΔH = −53 ± 5 kJ mol^{-1}) suggested that the transient helix (D217–G232) would fold further upon binding. Reversing the titration resulted in an N-value of 0.6, suggesting more than one binding site within the RIM2 ANAC013 fragment (Table 2). From an NMR titration, RIM2 displayed complex CSP movement suggesting two binding events, the second with a considerably weaker affinity. Since the same residues were affected, the second and much weaker binding event was possibly enabled by the first binding event (Supplementary Fig. S12). Disregarding this very weak interaction, an apparent K_D of 11 ± 2 μM was assumed for the RIM2 interaction with RCD1-RST (Table 2).

RIM1 and RIM2 have overlapping binding sites on RCD1-RST

We next asked whether the binding site for RIM2 on RCD1-RST would be different from that of RIM1. The resonances of RCD1-RST were previously assigned [28], and upon addition of ANAC013$_{161–274}$, we observed large CSPs (Supplementary Fig. S13), requiring reassignments (Supplementary Fig. S14). From adding either ANAC013$_{161–274}$ (RIM2 + RIM1) or ANAC013$_{254–274}$ (RIM1) to RCD1-RST, the CSPs were not markedly different (Fig. 3C). However, adding ANAC013$_{204–234}$ (RIM2) did affect similar resonances significantly, but with markedly lower amplitude, even considering the difference in affinities of over one order of magnitude (Fig. 3C and Supplementary Fig. S13). It also resulted in broader peaks suggesting an exchange on an intermediate to slow NMR timescale and prohibited the transfer of assignments of RCD1-RST L550–S572 to this bound state (Fig. 3C and Supplementary Fig. S13). Thus, these NMR data showed that the RIM1 and RIM2 binding sites on RCD1-RST are not identical, but overlap so much that simultaneous binding is prevented and therefore cannot give rise to cooperativity. To assess the population of the RIM1- and RIM2-bound states within the context of the long IDR in the ANAC013$_{161–274}$:RCD1-RST complex, we used a weighted average of the CSPs of W507-NH$^{\varepsilon 1}$ of RCD1-RST located within the binding site and positioned isolated in the NMR spectrum. From its CSPs in the ANAC013$_{254–274}$:RCD1-RST and ANAC013$_{204–234}$:RCD1-RST complexes, we obtained populations of 73% (RIM1-bound) and 27% (RIM2-bound), respectively, in a saturated ANAC013$_{161–274}$:RCD1-RST complex. Thus, there is a preference for RIM1 over RIM2, but not as extensive as the K D values obtained by ITC suggested (Table 2).

To obtain the thermodynamic parameters of the combined RIM2–RIM1 fragment, we performed titrations in both directions using ITC. With ANAC013$_{161–274}$ in the cell (Fig. 3A, right panel), we observed a biphasic isotherm with a distinct transition around the 1:1 ratio, but with sustained large heats after the first transition suggesting at least two binding events with orders of magnitude difference in affinity. The data could be fitted using a two-sets-of-sites model, producing N-values around 1. However, the fitted K_D values were an order of magnitude lower than what was obtained from the individual RIM titrations. Thus, binding cannot be explained by a sequential two-site binding model. In the reverse titration, we again obtained a biphasic isotherm (Supplementary Fig. S11A); however, here, we observed two distinct transitions at stoichiometries of around 0.4:1 and 0.7:1, and thus the quantitative interpretation and assignments of each transition were not clear (Table 2 and Supplementary Fig. S11A). The apparent mismatch between the two titrations was investigated by modeling the ITC experiments using the biochemical simu-

Table 2. Thermodynamic analyses of interactions between ANAC013 and RCD1-RST$_{499–572}$ using ITC

Cell	Syringe	K_D (nM)	N	ΔH (kJ mol^{-1})	$-T\Delta S$ (kJ mol^{-1})	ΔG (kJ mol^{-1})
ANAC013$_{254–274}$	RCD1-RST	70 ± 30	1.05 ± 0.05	−49 ± 5	8 + 5	−41 ± 1
ANAC013$_{204–234}$	RCD1-RST	11 000 ± 2000	0.87 ± 0.01	−53 ± 5	25 ± 5	−28.3 ± 0.3
ANAC013$_{161–274}$	RCD1-RST	1.6 ± 0.9	0.93 ± 0.07	−55 ± 4	5 ± 4	−50 ± 1
RCD1-RST	ANAC013$_{204–234}$	13 000 ± 2000	0.59 ± 0.02	−70 ± 4	42 ± 4	−27.9 ± 0.4
RCD1-RST	ANAC013$_{161–274}$	60 ± 30	0.68 ± 0.05	−20 ± 10	−20 ± 20	−41 ± 1
		13 ± 6	0.37 ± 0.04	−160 ± 40	120 ± 40	−45 ± 1
RCD1-RST	ANAC013$_{1–274}$	60 ± 30	0.63 ± 0.05	−19 ± 1	−22	−42
		14 ± 8	0.46 ± 0.08	−140 ± 5	95	−45

Errors represent standard deviations of at least three technical replicates.

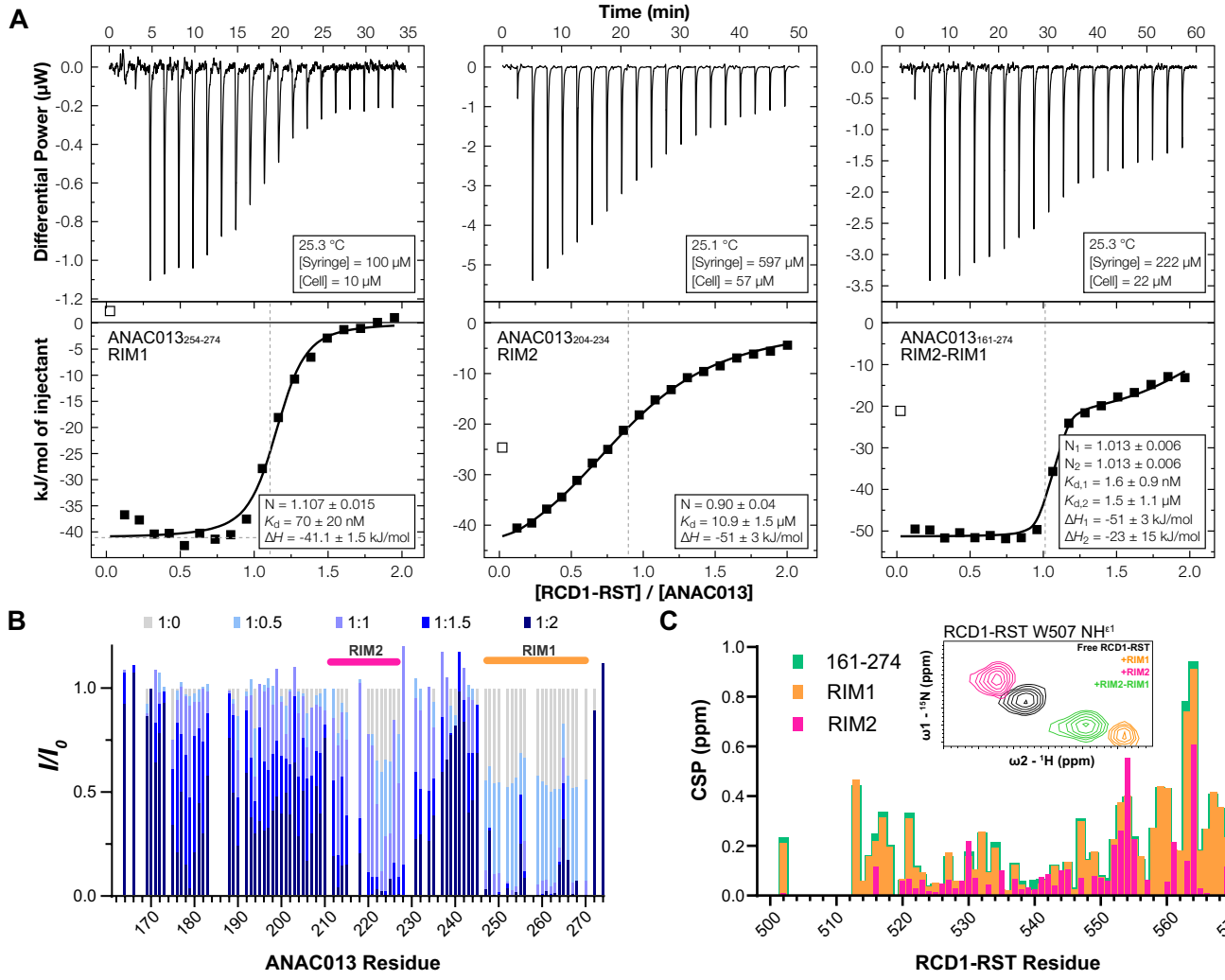

Figure 3. Interaction between ANAC013 and the negative regulator RCD1. (**A**) ITC data representative of the titration of RCD1-RST into ANAC013$_{254–274}$ (RIM1, left), ANAC013$_{204–234}$ (RIM2, middle), or ANAC013$_{161–274}$ (RIM2–RIM1, right). (**B**) Relative HSQC peak intensity profile (I/I_0) of ANAC013$_{161–274}$ with different ratios of RCD1-RST (1:0 to 1:2). (**C**) CSPs of RCD1-RST upon addition of saturating amounts of ANAC013$_{161–274}$ (green), RIM1 (orange), or RIM2 (pink). Inset: W507-NH$^{\varepsilon 1}$ region of the ^{1}H, ^{15}N HSQC spectrum of RCD1-RST in the same conditions.

lator COPASI [56] to obtain theoretical isotherms. The system was modeled as two independent binding sites. The simulations showed that the major features of both experimental isotherms could be obtained using a common set of parameters derived from the two-sets-of-sites fit of the experiment with ANAC013$_{161–274}$ in the cell (Fig. 3A, right panel), with $K_D$values approximately an order of magnitude lower than those determined for the individual RIM regions (Table 2 and Supplementary Fig. S11B). A plausible explanation for this discrepancy is that RIM1 and RIM2 are sequentially close (25 residues apart); therefore, the binding of RIM1 will cause an increase in the local effective concentration of RIM2 around RCD1-RST in the RIM1-bound state, and vice versa [57]. The probability of binding RIM2 will then be greatly increased in the time between dissociation of RIM1 to RST escape from the vicinity of the bivalent ANAC013 region.

Thus, the apparent affinity of both RIM1 and RIM2 will be enhanced through the phenomenon known as allovalency [46, 58–60].

Implementation of the allovalency model (Supplementary Fig. S11B) enabled reasonable recapitulation of the experimentally observed isotherms using parameters derived from the titrations of the individual sites. Therefore, our data support an allovalency model and indicate that individually described interactions are realistic in context of the full protein. However, some deviations from the ITC data and observed NMR peak intensity losses in the ANAC013 175–210 region (Fig. 3B) suggested that including minor states such as potential "trimers" (both RIMs bound at the same time) would be required to describe the multivalent ANAC013 interaction with RCD1-RST fully and accurately.

Discussion

Disregarding its transmembrane helix, the plant transcription factor ANAC013 has a conventional transcription factor architecture consisting of a folded DBD and a long IDR. Little is known about the intramolecular communication of ANAC013 and its functional impact. Using a high-throughput screening method, we identify three ADs in the IDR of ANAC013 and demonstrate that *in vitro* and in the context of the long IDR, only two of these ADs appear accessible. The remaining AD engages in larger assemblies within the C-terminus of the IDR with a high propensity for condensate formation [7, 61–63]. The three ADs locate to three out of four AIs. We show that two of these regions (AD1/AI2 and AD2/AI3) dynamically and electrostatically interact with the DBD. The core interaction sites based on the R_2 profiles correspond to $_{211}$FIEEEWAEDDDDDVDE$_{227}$ (AD1/AI2) and $_{250}$ELDDNDIEELMSQVRD$_{265}$ (AD2/AI3). Both display general AD features with aromatic and hydrophobic residues distributed among acidic residues enabling the display of hydrophobic residues suitable for interactions, as suggested by the recent acidic exposure model for transcription factor activation [5, 48]. A third AI, AI1, was found to fold onto the DBD in *trans* across the dimer, suggesting an extension to the folded NAC domain of ANAC013 compared to known NAC DBDs [54, 64]. The dynamic interactions of AD1/AI2 and AD2/AI3 with the positively charged residues of the DBD lead to an equilibrium in which 30% of the IDR population is bound to the DBD and 70% exists in an open state (Fig. 4). Thus, the ADs of the ANAC013 IDR remain accessible in a dynamic equilibrium between open and closed states.

Overlapping with—but not identical to—the AD/AIs, the IDR is bound to the RST domain of the negative regulator RCD1 through two different sites, RIM1 and RIM2 (Fig. 1A). We observed that RCD1-RST bound the IDR, both in the absence and in the presence of DNA, and did so allovalently with affinities unperturbed by DNA using two sites positioned vis-à-vis (Fig. 4A). Allovalency requires multivalency, given as several identical or similar sites that bind one at a time to the same site on the target protein. After dissociation, rebinding of another spatially close site prevents escape from the binding partner. The increase in time spent in the bound state leads to sensitive dependence on the number of binding sites, increasing the apparent K_D with the number of sites [60, 65]. Allovalency has, because of its mathematical description [58, 66], predictive power. Thus, the allovalency model introduces an intermediary state, where the interaction partner is localized within proximity to the multivalent binding region. The transition between the captured and the free diffusing states is controlled by several factors: the spatial distance between the binding regions, the diffusion coefficients of the interacting proteins, and the competing probabilities of the partner protein binding to an accessible site versus diffusing out of the effective range, referred to as the "capture sphere". Within this capture sphere, the association rate constant will depend on the local effective concentration, c_{eff}, of the interaction partner (Fig. 4A) [46, 58, 66].

Importantly, RCD1-RST is bound by only partially disrupting the electrostatic contacts between the AD/AIs in the IDR and the DBD, suggesting that the interactions with the DBD and with RCD1-RST locate to the same regions but are not completely overlapping (Fig. 2E and G). Indeed, ANAC013$_{1–274}$ can bind target DNA when already bound to RCD1-RST, and vice versa. These results therefore suggest that regulation of ANAC013 by RCD1 works not to prevent DNA binding, but rather to scavenge its ADs that overlap with the RIMs, dynamically. Thus, scavenging of AD1/AI2 and AD2/AI3 by RCD1 would compete with binding of coactivators both with and without DNA bound (Fig. 4B). Binding the two ADs allovalently to RCD1-RST will provide dynamic access to one unbound AD and thereby allow for takeover by another coregulator when its concentration increases. It is also possible that activators may be specific to a single site, either AD1 or AD2, and thus will be unable to exploit the additional binding strength arising from allovalency. Importantly, this is regulated by the relative levels of the partners, and at low transcription factor concentration, both sites will be occupied by RCD1-RST and transcription then effectively turned off, independently of the presence of DNA.

In agreement with previous studies on SOX2 [12], we found that the affinity for DNA was not affected by the presence of the IDR. Surprisingly, the interdomain interaction did not affect ANAC013 affinity for its negative regulator RCD1-RST either. Thus, other functions relevant for this interdomain interaction must exist. Intriguingly, we observed that the interdomain communication lowered the entropic barrier for DNA binding by contributing with favorable entropy related to chain release. Such an entropic driving force has been seen in other IDR-driven interactions, e.g. by release of the C-terminal tail of RST upon DREB2A binding [29], or the differential binding of MKK4 to p38α or JNK1 [67]. Furthermore, the release of the IDRs from the DBD by DNA was independent of DNA sequence. Thus, the mere presence of DNA expels the IDR from the DBD, modulating the equilibrium between open and closed states. This suggests that, unlike an autoinhibition of DNA binding from acidic stretches and from phosphorylation observed in e.g. p53 [9, 11], even nonspecific DNA will prime the ANAC013 DBD for DNA binding [52–54], and other negatively charged molecules such as RNA, polyphosphate, or negatively charged binding partners may induce similar effects. It is also possible that the interdomain interaction within ANAC013 serves to regulate coactivator binding. Possibly, some coactivators bind to the closed form and others to the open form, effectively serving as a filter for binding. For now, effects from different relevant binding partners, including RNA, remain to be addressed.

Our work raises an important implication for transcription factors with more than one AD, whose abundance is becoming evident through the vast information from the many high-throughput studies emerging. Since allovalency requires the

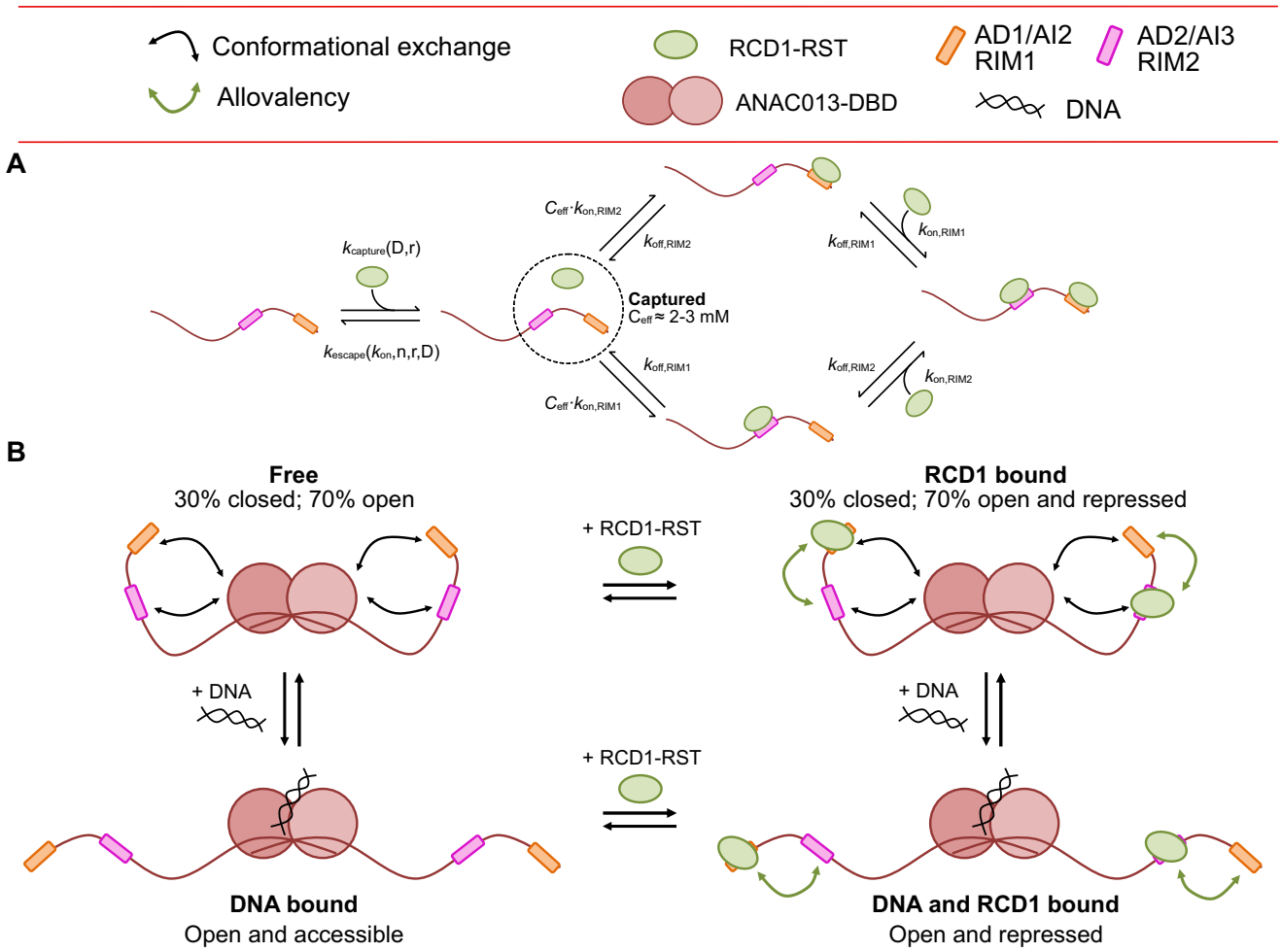

Figure 4. Allovalent scavenging of ADs gears transcription factors for activation. (**A**) Model of the RCD1-RST interaction with the two RIM motifs in ANAC013. The capture rate depends on the number of binding sites, *n*, the diffusion coefficients, *D*, and a sphere with a radius *r* that depends on the mean distance between binding sites [46]. The escape rate further depends on the number of sites and the association rate constant that governs the probability of association versus the probability of escape. The effective concentration (c_{eff}) can be determined as the concentration of a single particle in the sphere or using more empirical approaches. (**B**) In DNA-free ANAC013, its IDR interacts with the DBD through AD1/AI2 and AD2/AI3, in equilibrium between a 30% closed form and a 70% open form (top left) occupying the ADs. Upon the presence of DNA, the AIs are released, shifting the equilibrium toward the open form (bottom left). RCD1-RST can interact allovalently with either free or DNA-bound ANAC013, through RIM1 and RIM2, leading to dynamic occupation at enhanced affinity (top and bottom right).

ADs to be closely positioned within the sequence, the distance between ADs within the same transcription factor now becomes relevant for inferring how they are regulated. In the case of closely positioned ADs, allovalent and dynamic exchange of regulators represents a mechanism for fast regulation, complementing those suggested for frustration-based coregulator exchange [23], as well as those involving trimer formation, including HIF1α and CITED2 competition for TAZ1 [68, 69], and prothymosin α and histone H1 [70], involving competitive substitution [71].

Conclusion

In summary, we identify intramolecular interactions between the DBD of the transcription factor ANAC013 and ADs/AIs located in its IDR. These interactions are released by DNA and do not affect the affinity of ANAC013 for its target DNA or for its negative regulator RCD1. We demonstrate that interactions with DNA and RCD1 are not mutually exclusive but use sites that partially overlap and that two ADs/AIs in the IDR are efficiently scavenged by the RST domain of RCD1 through allovalency. Thus, ANAC013 regulation by intramolecular communication is not aimed at preventing DNA binding, but rather at modulating access to its ADs. The data support an allovalency model for regulation of the transcription factor ANAC013 by its negative regulator RCD1, where ADs are dynamically and efficiently scavenged. The model may be relevant for other transcription factor systems harboring closely positioned ADs within their IDR.

Acknowledgements

We acknowledge DESY (Hamburg, Germany), a member of the Helmholtz Association HGF, for the provision of experimental facilities. The synchrotron SAXS data were collected at beamline P12 operated by EMBL Hamburg at the PETRA III storage ring (DESY, Hamburg, Germany). We would like to thank Cy Jeffries for the assistance in using the beamline. Beam time was allocated for proposal SAXS-1279 (PI Annette E. Langkilde). We acknowledge Signe Agernæs Sjørup

for skilled technical assistance in the lab, Andreas Prestel for NMR assistance, and Johan G. Olsen for discussion on the AlphaFold structure.

Author contributions: E.D., B.B.K., and K.S. designed experiments. E.D. and C.O.S. prepared proteins. E.D. carried out and analyzed NMR and SAXS experiments. E.D. and A.D.D. carried out and analyzed ITC experiments. E.D. and F.F.T. carried out the RIM2 binding analyses by ITC and NMR, and F.F.T. modeled the complex allovalent binding isotherms. N.M. and L.C.S carried out and analyzed high-throughput transcriptional activation experiments. M.B. and E.D. carried out flexible-meccano ensemble generation and analysis. E.D., K.S., and B.B.K. wrote the manuscript and incorporated comments from all authors.

Supplementary data

Supplementary data is available at NAR online.

Conflict of interest

None declared.

Funding

This work was supported by the Novo Nordisk Foundation challenge grant REPIN, rethinking protein interactions (grant no. NNF18OC0033926, to B.B.K. and K.S.) and by the Danish Research Councils (grant no. 9040-00164B to B.B.K. and K.S.). NMR spectra were recorded at cOpenNMR, an infrastructure supported by the Novo Nordisk Foundation (grant no. NNF18OC0032996) and we thank Villumfonden for supporting the NMR facility. Activation domain assay was done under the National Science Foundation (NSF) (PGRP BIO-2112056 to L.C.S.; Postdoctoral Research Program IOS-1907098 to N.M.). Funding to pay the Open Access publication charges for this article was provided by Novo Nordisk Foundation grant no. NNF18OC0033926 and Danish Research Councils grant no. 9040-00164B.

Data availability

NMR assignments were deposited in the BioMagResBank (BMRB) with accession numbers 51969 ($ANAC013_{161–274}$) and 51970 (RCD1-RST bound to $ANAC013_{161–274}$). SAXS data have been uploaded to sasdb.org (accession numbers SASDU27 and SASDU37) and are freely available.

References

1. Staby L, O'Shea C, Willemoës M *et al.* Eukaryotic transcription factors: paradigms of protein intrinsic disorder. *Biochem J* 2017;**474**:2509–32. https://doi.org/10.1042/BCJ20160631
2. van der LR, Buljan M, Lang B *et al.* Classification of intrinsically disordered regions and proteins. *Chem Rev* 2014;**114**:6589–631. https://doi.org/10.1021/cr400525m
3. Babu MM, van der Lee R, de Groot NS *et al.* Intrinsically disordered proteins: regulation and disease. *Curr Opin Struct Biol* 2011;**21**:432–40. https://doi.org/10.1016/j.sbi.2011.03.011
4. Staller MV, Holehouse AS, Swain-Lenz D *et al.* A high-throughput mutational scan of an intrinsically disordered acidic transcriptional activation domain. *Cell Syst* 2018;**6**:444–55. https://doi.org/10.1016/j.cels.2018.01.015
5. Erijman A, Kozlowski L, Sohrabi-Jahromi S *et al.* A high-throughput screen for transcription activation domains reveals their sequence features and permits prediction by deep learning. *Mol Cell* 2020;**78**:890–902.https://doi.org/10.1016/j.molcel.2020.04.020
6. Morffy N, Van den Broeck L, Miller C *et al.* Identification of plant transcriptional activation domains. *Nature* 2024;**632**:166–73. https://doi.org/10.1038/s41586-024-07707-3
7. Boija A, Klein IA, Sabari BR *et al.* Transcription factors activate genes through the phase-separation capacity of their activation domains. *Cell* 2018;**175**:1842–55. https://doi.org/10.1016/j.cell.2018.10.042
8. Holehouse AS, Kragelund BB . The molecular basis for cellular function of intrinsically disordered protein regions. *Nat Rev Mol Cell Biol* 2024;**25**:187–211. https://doi.org/10.1038/s41580-023-00673-0
9. Krois AS, Dyson HJ, Wright PE. Long-range regulation of p53 DNA binding by its intrinsically disordered N-terminal transactivation domain. *Proc Natl Acad Sci USA* 2018;**115**:E11302–10. https://doi.org/10.1073/pnas.1814051115
10. He F, Borcherds W, Song T *et al.* Interaction between p53 N terminus and core domain regulates specific and nonspecific DNA binding. *Proc Natl Acad Sci USA* 2019;**116**:8859–68. https://doi.org/10.1073/pnas.1903077116
11. Sun X, Dyson HJ, Wright PE. A phosphorylation-dependent switch in the disordered p53 transactivation domain regulates DNA binding. *Proc Natl Acad Sci USA* 2021;**118**:e2021456118. https://doi.org/10.1073/pnas.2021456118
12. Bjarnason S, McIvor JAP, Prestel A *et al.* DNA binding redistributes activation domain ensemble and accessibility in pioneer factor Sox2. *Nat Commun* 2024;**15**:1445. https://doi.org/10.1038/s41467-024-45847-2
13. Kragelund BB, Jensen MK, Skriver K. Order by disorder in plant signaling. *Trends Plant Sci* 2012;**17**:625–32. https://doi.org/10.1016/j.tplants.2012.06.010
14. De Clercq I, Vermeirssen V, Van Aken O *et al.* The membrane-bound NAC transcription factor ANAC013 functions in mitochondrial retrograde regulation of the oxidative stress response in *Arabidopsis*. *Plant Cell* 2013;**25**:3472–90. https://doi.org/10.1105/tpc.113.117168
15. Jurdak R, Launay-Avon A, Paysant-Le Roux C *et al.* Retrograde signalling from the mitochondria to the nucleus translates the positive effect of ethylene on dormancy breaking of *Arabidopsis thaliana* seeds. *New Phytol* 2021;**229**:2192–205. https://doi.org/10.1111/nph.16985
16. Shapiguzov A, Vainonen JP, Hunter K *et al. Arabidopsis* RCD1 coordinates chloroplast and mitochondrial functions through interaction with ANAC transcription factors. *eLife* 2019;**8**:e43284. https://doi.org/10.7554/eLife.43284
17. Teotia S, Lamb RS. The paralogous genes RADICAL-INDUCED CELL DEATH1 and SIMILAR TO RCD ONE1 have partially redundant functions during *Arabidopsis* development. *Plant Physiol* 2009;**151**:180–98. https://doi.org/10.1104/pp.109.142786
18. Jaspers P, Blomster T, Brosché M *et al.* Unequally redundant RCD1 and SRO1 mediate stress and developmental responses and interact with transcription factors. *Plant J* 2009;**60**:268–79. https://doi.org/10.1111/j.1365-313X.2009.03951.x
19. Staby L, Bugge K, Falbe-Hansen RG *et al.* Connecting the αα-hubs: same fold, disordered ligands, new functions. *Cell Commun Signal* 2021;**19**:2. https://doi.org/10.1186/s12964-020-00686-8
20. Bugge K, Staby L, Salladini E *et al.* αα-hub domains and intrinsically disordered proteins: a decisive combo. *J Biol Chem* 2021;**296**:100226. https://doi.org/10.1074/jbc.REV120.012928
21. O'Shea C, Staby L, Bendsen SK *et al.* Structures and short linear motif of disordered transcription factor regions provide clues to the interactome of the cellular hub protein radical-induced cell death1. *J Biol Chem* 2017;**292**:512–27. https://doi.org/10.1074/jbc.M116.753426

22. Christensen LF, Staby L, Bugge K *et al.* Evolutionary conservation of the intrinsic disorder-based Radical-Induced Cell Death1 hub interactome. *Sci Rep* 2019;**9**:18927.https://doi.org/10.1038/s41598-019-55385-3
23. Theisen FF, Prestel A, Elkjær S *et al.* Molecular switching in transcription through splicing and proline-isomerization regulates stress responses in plants. *Nat Commun* 2024;**15**:592. https://doi.org/10.1038/s41467-024-44859-2
24. Vainonen JP, Jaspers P, Wrzaczek M *et al.* RCD1–DREB2A interaction in leaf senescence and stress responses in *Arabidopsis thaliana*. *Biochem J* 2012;**442**:573–81. https://doi.org/10.1042/BJ20111739
25. Studier FW. Protein production by auto-induction in high density shaking cultures. *Protein Expr Purif* 2005;**41**:207–34. https://doi.org/10.1016/j.pep.2005.01.016
26. Pedersen CP, Seiffert P, Brakti I *et al.* Production of intrinsically disordered proteins for biophysical studies: tips and tricks. *Methods Mol Biol* 2020;**2141**:195–209. https://doi.org/10.1007/978-1-0716-0524-0_9
27. Singh KK, Graether SP. Expression and purification of an intrinsically disordered protein. *Methods Mol Biol* 2020;**2141**:181–94. https://doi.org/10.1007/978-1-0716-0524-0_8
28. Bugge K, Staby L, Kemplen KR *et al.* Structure of radical-induced cell death1 hub domain reveals a common αα-scaffold for disorder in transcriptional networks. *Structure* 2018;**26**:734–46. https://doi.org/10.1016/j.str.2018.03.013
29. Staby L, Due AD, Kunze MBA *et al.* Flanking disorder of the folded αα-hub domain from radical induced cell death1 affects transcription factor binding by ensemble redistribution. *J Mol Biol* 2021;**433**:167320. https://doi.org/10.1016/j.jmb.2021.167320
30. Solyom Z, Schwarten M, Geist L *et al.* BEST-TROSY experiments for time-efficient sequential resonance assignment of large disordered proteins. *J Biomol NMR* 2013;**55**:311–21. https://doi.org/10.1007/s10858-013-9715-0
31. Hyberts SG, Takeuchi K, Wagner G. Poisson-gap sampling and forward maximum entropy reconstruction for enhancing the resolution and sensitivity of protein NMR data. *J Am Chem Soc* 2010;**132**:2145–7. https://doi.org/10.1021/ja908004w
32. Orekhov VY, Jaravine VA. Analysis of non-uniformly sampled spectra with multi-dimensional decomposition. *Prog Nucl Magn Reson Spectrosc* 2011;**59**:271–92. https://doi.org/10.1016/j.pnmrs.2011.02.002
33. Lee W, Rahimi M, Lee Y *et al.* POKY: a software suite for multidimensional NMR and 3D structure calculation of biomolecules. *Bioinformatics* 2021;**37**:3041–2. https://doi.org/10.1093/bioinformatics/btab180
34. Jung YS, Zweckstetter M. Mars—robust automatic backbone assignment of proteins. *J Biomol NMR* 2004;**30**:11–23. https://doi.org/10.1023/B:JNMR.0000042954.99056.ad
35. Wirmer J, Wolfgang P, Schwalbe H. Motional properties of unfolded ubiquitin: a model for a random coil protein. *J Biomol NMR* 2006;**35**:175–86. https://doi.org/10.1007/s10858-006-9026-9
36. Mulder FAA, Schipper D, Bott R *et al.* Altered flexibility in the substrate-binding site of related native and engineered high-alkaline *Bacillus subtilisins*. *J Mol Biol* 1999;**292**:111–23. https://doi.org/10.1006/jmbi.1999.3034
37. Nielsen JT, Mulder FAA. POTENCI: prediction of temperature, neighbor and pH-corrected chemical shifts for intrinsically disordered proteins. *J Biomol NMR* 2018;**70**:141–65. https://doi.org/10.1007/s10858-018-0166-5
38. Kjaergaard M, Poulsen FM. Sequence correction of random coil chemical shifts: correlation between neighbor correction factors and changes in the Ramachandran distribution. *J Biomol NMR* 2011;**50**:157–65. https://doi.org/10.1007/s10858-011-9508-2
39. Blanchet CE, Spilotros A, Schwemmer F *et al.* Versatile sample environments and automation for biological solution X-ray scattering experiments at the P12 beamline (PETRA III, DESY). *J Appl Crystallogr* 2015;**48**:431–43. https://doi.org/10.1107/S160057671500254X
40. Petoukhov MV, Franke D, Shkumatov AV *et al.* New developments in the ATSAS program package for small-angle scattering data analysis. *J Appl Crystallogr* 2012;**45**:342–50. https://doi.org/10.1107/S0021889812007662
41. Ozenne V, Bauer F, Salmon L *et al.* Flexible-meccano: a tool for the generation of explicit ensemble descriptions of intrinsically disordered proteins and their associated experimental observables. *Bioinformatics* 2012;**28**:1463–70. https://doi.org/10.1093/bioinformatics/bts172
42. Bernadó P, Blanchard L, Timmins P *et al.* A structural model for unfolded proteins from residual dipolar couplings and small-angle X-ray scattering. *Proc Natl Acad Sci USA* 2005;**102**:17002–7. https://doi.org/10.1073/pnas.0506202102
43. Svergun D, Barberato C, Koch MH. CRYSOL—a program to evaluate X-ray solution scattering of biological macromolecules from atomic coordinates. *J Appl Crystallogr* 1995;**28**:768–73.
44. Mirdita M, Schütze K, Moriwaki Y *et al.* ColabFold: making protein folding accessible to all. *Nat Methods* 2022;**19**:679–82. https://doi.org/10.1038/s41592-022-01488-1
45. Konarev PV, Volkov VV, Sokolova AV *et al.* PRIMUS: a Windows PC-based system for small-angle scattering data analysis. *J Appl Crystallogr* 2003;**36**:1277–82. https://doi.org/10.1107/S0021889803012779
46. Klein P, Pawson T, Tyers M. Mathematical modeling suggests cooperative interactions between a disordered polyvalent ligand and a single receptor site. *Curr Biol* 2003;**13**:1669–78. https://doi.org/10.1016/j.cub.2003.09.027
47. O'Shea C, Kryger M, Stender EGP *et al.* Protein intrinsic disorder in *Arabidopsis* NAC transcription factors: transcriptional activation by ANAC013 and ANAC046 and their interactions with RCD1. *Biochem J* 2015;**465**:281–94. https://doi.org/10.1042/BJ20141045
48. Staller MV, Ramirez E, Kotha SR *et al.* Directed mutational scanning reveals a balance between acidic and hydrophobic residues in strong human activation domains. *Cell Syst* 2022;**13**:334–45. https://doi.org/10.1016/j.cels.2022.01.002
49. Millard PS, Bugge K, Marabini R *et al.* IDDomainSpotter: compositional bias reveals domains in long disordered protein regions—insights from transcription factors. *Protein Sci* 2020;**29**:169–83. https://doi.org/10.1002/pro.3754
50. Chu X, Sun T, Li Q *et al.* Prediction of liquid–liquid phase separating proteins using machine learning. *BMC Bioinformatics* 2022;**23**:72. https://doi.org/10.1186/s12859-022-04599-w
51. Ibrahim AY, Khaodeuanepheng NP, Amarasekara DL *et al.* Intrinsically disordered regions that drive phase separation form a robustly distinct protein class. *J Biol Chem* 2023;**299**:102801. https://doi.org/10.1016/j.jbc.2022.102801
52. Spera S, Bax A. Empirical correlation between protein backbone conformation and Cα and Cβ ^{13}C nuclear magnetic resonance chemical shifts. *J Am Chem Soc* 1991;**113**:5490–92. https://doi.org/10.1021/ja00014a071
53. Chun I, Kim HJ, Hong S *et al.* Structural basis of DNA binding by the NAC transcription factor ORE1, a master regulator of plant senescence. *Plant Commun* 2023;**4**:100510. https://doi.org/10.1016/j.xplc.2022.100510
54. Welner DH, Lindemose S, Grossmann JG *et al.* DNA binding by the plant-specific NAC transcription factors in crystal and solution: a firm link to WRKY and GCM transcription factors. *Biochem J* 2012;**444**:395–404. https://doi.org/10.1042/BJ20111742
55. Skriver K, Theisen FF, Kragelund BB. Conformational entropy in molecular recognition of intrinsically disordered proteins. *Curr Opin Struct Biol* 2023;**83**:102697. https://doi.org/10.1016/j.sbi.2023.102697
56. Hoops S, Gauges R, Lee C *et al.* COPASI—a COmplex PAthway SImulator. *Bioinformatics* 2006;**22**:3067–74. https://doi.org/10.1093/bioinformatics/btl485

57. Sørensena CS, Kjaergaarda M. Effective concentrations enforced by intrinsically disordered linkers are governed by polymer physics. *Proc Natl Acad Sci USA* 2019;**116**:23124–31. https://doi.org/10.1073/pnas.1904813116
58. Locasale JW. Allovalency revisited: an analysis of multisite phosphorylation and substrate rebinding. *J Chem Phys* 2008;**128**:115106. https://doi.org/10.1063/1.2841124
59. Olsen JG, Teilum K, Kragelund BB. Behaviour of intrinsically disordered proteins in protein–protein complexes with an emphasis on fuzziness. *Cell Mol Life Sci* 2017;**74**: 3175–83. https://doi.org/10.1007/s00018-017-2560-7
60. Mittag T, Marsh J, Grishaev A *et al.* Structure/function implications in a dynamic complex of the intrinsically disordered Sic1 with the Cdc4 subunit of an SCF ubiquitin ligase. *Structure* 2010;**18**:494–506. https://doi.org/10.1016/j.str.2010.01.020
61. Garcia DA, Johnson TA, Presman DM *et al.* An intrinsically disordered region-mediated confinement state contributes to the dynamics and function of transcription factors. *Mol Cell* 2021;**81**:1484–98. https://doi.org/10.1016/j.molcel.2021.01.013
62. Wagh K, Garcia DA, Upadhyaya A. Phase separation in transcription factor dynamics and chromatin organization. *Curr Opin Struct Biol* 2021;**71**:148–55. https://doi.org/10.1016/j.sbi.2021.06.009
63. Hahn S. Phase separation, protein disorder, and enhancer function. *Cell* 2018;**175**:1723–25. https://doi.org/10.1016/j.cell.2018.11.034
64. Ernst HA, Olsen AN, Skriver K *et al.* Structure of the conserved domain of ANAC, a member of the NAC family of transcription factors. *EMBO Rep* 2004;**5**:297–303. https://doi.org/10.1038/sj.embor.7400093
65. Hayama R, Sparks S, Hecht LM *et al.* Thermodynamic characterization of the multivalent interactions underlying rapid and selective translocation through the nuclear pore complex. *J Biol Chem* 2018;**293**:4555–63. https://doi.org/10.1074/jbc.AC117.001649
66. Levchenko A. Allovalency: a case of molecular entanglement. *Curr Biol* 2003;**13**:R876–78. https://doi.org/10.1016/j.cub.2003.10.049
67. Kragelj J, Ozenne V, Blackledge M *et al.* Conformational propensities of intrinsically disordered proteins from NMR chemical shifts. *ChemPhysChem* 2013;**14**:3034–45. https://doi.org/10.1002/cphc.201300387
68. Berlow RB, Dyson HJ, Wright PE. Hypersensitive termination of the hypoxic response by a disordered protein switch. *Nature* 2017;**543**:447–51. https://doi.org/10.1038/nature21705
69. Berlow RB, Martinez-Yamout MA, Dyson HJ *et al.* Role of backbone dynamics in modulating the interactions of disordered ligands with the TAZ1 domain of the CREB-binding protein. *Biochemistry* 2019;**58**:1354–62. https://doi.org/10.1021/acs.biochem.8b01290
70. Borgia A, Borgia MB, Bugge K *et al.* Extreme disorder in an ultrahigh-affinity protein complex. *Nature* 2018;**555**:61–66. https://doi.org/10.1038/nature25762
71. Sottini A, Borgia A, Borgia MB *et al.* Polyelectrolyte interactions enable rapid association and dissociation in high-affinity disordered protein complexes. *Nat Commun* 2020;**11**:5736. https://doi.org/10.1038/s41467-020-18859-x
72. Ward JJ, McGuffin LJ, Bryson K *et al.* The DISOPRED server for the prediction of protein disorder. *Bioinformatics* 2004;**20**:2138–39. https://doi.org/10.1093/bioinformatics/bth195

Received: April 17, 2024. **Revised:** January 18, 2025. **Editorial Decision:** January 20, 2025. **Accepted:** January 23, 2025